The role of the water vapor feedback in the ITCZ response to hemispherically asymmetric forcings

Spencer K. Clark*

Program in Atmospheric and Oceanic Sciences, Princeton University, Princeton, New Jersey

Yi Ming, Isaac M. Held, and Peter J. Phillipps

Geophysical Fluid Dynamics Laboratory/NOAA, Princeton, New Jersey

**Corresponding author address:* Program in Atmospheric and Oceanic Sciences, Princeton University, 219 Sayre Hall 300 Forrestal Road, Princeton, NJ, USA.

E-mail: skclark@princeton.edu

ABSTRACT

In comprehensive and idealized general circulation models, hemispherically asymmetric forcings lead to shifts in the latitude of the Intertropical Convergence Zone (ITCZ). Prior studies using comprehensive GCMs (with complicated parameterizations of radiation, clouds, and convection) suggest that the water vapor feedback tends to amplify the movement of the ITCZ in response to a given hemispherically asymmetric forcing, but this effect has yet to be elucidated in isolation. This study uses an idealized moist model, coupled to a full radiative transfer code, but without clouds, to examine the role of the water vapor feedback in a targeted manner.

In experiments with interactive water vapor and radiation, the ITCZ latitude shifts roughly twice as much off the equator as in cases with the water vapor field seen by the radiation code prescribed to a static hemisperically-symmetric control distribution. Using energy flux equator theory for the latitude of the ITCZ, the amplification of the ITCZ shift is attributed primarily to the longwave water vapor absorption associated with the movement of the ITCZ into the warmer hemisphere, further increasing the net column heating asymmetry. Local amplification of the imposed forcing by the shortwave water vapor feedback plays a secondary role. Experiments varying the convective relaxation time, an important parameter in the convection scheme used in the idealized moist model, yield qualitatively similar results, suggesting some degree of robustness to the model physics; however, the sensitivity experiments do not preclude that more extreme modifications to the convection scheme could lead to qualitatively different behavior.

1. Introduction

It has been shown in numerous studies using both idealized and comprehensive general circulation models (GCMs) that the zonal and annual mean latitude of the intertropical convergence zone (ITCZ) changes in response to hemispherically asymmetric perturbations to the energy budget. By hemispherically asymmetric, we mean the perturbations on one side of the equator are substantially different than those on the other. In the real world, these perturbations can enter the system in a wide variety of ways, including anomalous ocean heat fluxes into or out of the atmosphere (e.g. Kang et al. 2008, 2009; Cvijanovic and Chiang 2012; Donohoe et al. 2013; Seo et al. 2014; Bischoff and Schneider 2014, 2015), changes in the surface albedo (e.g. Chiang and Bitz 2005; Voigt et al. 2013), or changes in the aerosol concentrations that can directly scatter/absorb shortwave radiation and/or indirectly alter the radiative properties of clouds (e.g. Yoshioka et al. 2007; Yoshimori and Broccoli 2008; Ming and Ramaswamy 2011; Clark et al. 2015).

The direction of the shift in the ITCZ position is towards the hemisphere receiving comparatively more energy (Donohoe et al. 2013); this is consistent with the seasonally varying position of the ITCZ (Huffman et al. 2009), which migrates from the NH in boreal summer to the SH in boreal winter. While the direction of the shift follows a consistent pattern in modeling studies, the magnitude of the shift has been shown to depend strongly on the strength and location of the asymmetric perturbation and the treatment of physical processes in a particular model (Kang et al. 2009; Voigt et al. 2013, 2014; Seo et al. 2014).

This dependency on the inclusion or exclusion of physical processes is illustrated by the results of Kang et al. (2009) and Seo et al. (2014). In both of these studies, hemispherically antisymmetric patterns of slab ocean heat flux were prescribed in both comprehensive aquaplanet GCMs, complete with water vapor and cloud feedbacks, and idealized moist GCMs, without water vapor or cloud feedbacks. In each study, the ITCZ latitude was more sensitive to a given asymmetry strength in the comprehensive aquaplanet GCM than in the idealized moist GCM. In addition, in the comprehensive GCM, an asymmetry imposed in the extratropics was more effective at shifting the ITCZ than an asymmetry imposed in the tropics, but the opposite was true in the idealized GCM.

Voigt et al. (2013) imposed hemispherically antisymmetric perturbations to surface albedo in a comprehensive aquaplanet GCM with water vapor and cloud feedbacks; in their case, using one convection scheme, the magnitude of the ITCZ shift in response to a given albedo asymmetry did not change when switching from interactive cloud radiative effect (CRE) to prescribed CRE, but with another convection scheme, the ITCZ shifted more with interactive CRE. Voigt et al. (2013) argue that the difference in sensitivity between the two simulations results from differences in the net radiative effect of clouds associated with the ITCZ, which can be traced back to the convection scheme used. When the clouds had a roughly net zero effect on the net radiation at top of atmosphere (TOA), there was little difference between the interactive and "locked" clouds experiments, but when the clouds had a net positive effect on the net radiation at TOA, the ITCZ shifted more with interactive clouds than with prescribed clouds.

The examples above demonstrate the importance of the treatment of physical processes in setting the sensitivity of the ITCZ position to hemispherically asymmetric perturbations. In the context of radiation and the energy budget of the atmosphere, clouds and water vapor are the two most important spatially-heterogeneous factors to consider (Hartmann 2016). In terms of physical processes, previous studies have either included both cloud and water vapor radiative feedbacks, by using comprehensive aquaplanet GCMs, or included neither, by using models with gray radiative transfer using prescribed shortwave and longwave optical depths. That being said, while the parameterization of clouds and convection in atmospheric models remains a challenge, and varies from model to model (Boucher et al. 2013), the interaction between water vapor and radiation is better understood and more consistently represented (Held and Soden 2000, 2006). Therefore, there is reason to believe that the role of water vapor in determining the ITCZ latitude could be more robust than that for clouds.

It has been demonstrated by applying radiative feedback analysis to simulations conducted with comprehensive GCMs that the longwave greenhouse effect of the water vapor maximum associated with the ITCZ acts to amplify a latitudinal shift of the ITCZ to a given asymmetric perturbation (Yoshimori and Broccoli 2009; Frierson and Hwang 2011). Additional studies have also touched upon the role of the water vapor feedback in influencing ITCZ shifts (e.g. Cvijanovic and Chiang 2012; Cvijanovic et al. 2013; Voigt et al. 2013), but a targeted study of the role of water vapor in setting the sensitivity of the ITCZ latitude to the location and magnitude of hemispherically asymmetric perturbations, with only water vapor, full radiation, and convection as the primary model atmospheric physics components, has yet to be completed.

In this study, we use a new version of an idealized moist GCM, based on the model introduced in Frierson et al. (2006), coupled to a full radiative transfer code to capture the interaction between water vapor, radiation, and the circulation of the atmosphere in the absence of clouds (described in Sections 2 and 3). With this model we apply negative perturbations to the incoming solar radiation in the NH tropics or extratropics, in configurations analogous to the “free” and “locked” clouds experiments in Voigt et al. (2013) – this time with the water vapor field seen by the radiation code “free” or “locked” (Section 4a). Given that Voigt et al. (2013) found that the sensitivity of the ITCZ latitude to hemispherically asymmetric perturbations varied even with prescribed CRE when the convection scheme was changed, it is possible that the role of water vapor-radiation interaction may also be sensitive to the convection scheme used. Therefore, to test the sensitivity to changes in the convection scheme, we run analogous experiments while varying the convective relaxation time (τ_{SBM}), an important parameter for the convection scheme in this particular model (Frierson 2007), through modest and extreme values (Section 4b). We discuss these results in the context of prior work in Section 5 and conclude in Section 6.

2. Methods

a. Model Description and Control Simulations

All experiments in this study are performed using an idealized moist GCM. This model was introduced in Frierson et al. (2006) and Frierson et al. (2007), and was later modified to include a simplified Betts-Miller parameterization of convection (Frierson 2007). The behavior of this convection scheme is strongly dependent on the convective relaxation time (τ_{SBM}), which prescribes a timescale over which the ambient profiles of temperature and humidity are relaxed to reference convectively adjusted states (Frierson 2007). As described in Merlis et al. (2012), in models of this type, when water vapor condenses through large scale processes or the convection scheme, latent heat is released and the condensed water falls out instantaneously as rain. At the surface, the model is coupled to a slab ocean, which we set to have a depth of one meter for fast equilibration.

Surface fluxes and boundary layer mixing are determined similarly to the way they were in Frierson et al. (2006), with some minor distinctions. Instead of using the same drag coefficients for momentum, temperature, and water vapor, we use differing ones depending on the quantity. In determining those coefficients, roughness lengths of 5×10^{-3} m, 1×10^{-5} m, and 1×10^{-5} m are used respectively; these are the same values that were used in O'Gorman and Schneider (2008). In addition, unlike in Frierson et al. (2006), the formulation of the drag coefficients differs between neutral and unstable conditions (Dyer 1974), and we use a critical Richardson number of 2.0 rather than 1.0.

Radiative transfer was initially kept simple in the model. The atmosphere was transparent to shortwave radiation and "gray" (optical depth independent of wavelength) with respect to longwave radiation. Specifically, a longwave optical depth, varying with latitude and height, was prescribed to approximate the static impact of water vapor on radiative heating and cooling rates in the atmosphere (Frierson et al. 2006). As such, feedbacks involving the radiative impact of water vapor were not considered as the longwave optical depth would remain constant at the prescribed value, regardless of the specific humidity in the model.

To allow for the water vapor-radiation feedback, we replace the gray-atmosphere scheme with a comprehensive radiative transfer code (Paynter and Ramaswamy 2014). A similar setup was used in Merlis et al. (2012) to study the response of the Hadley circulation to orbital precession. Since condensed water leaves the atmosphere immediately as rain, there are no parameterizations of clouds in the model, and therefore no interactively-simulated cloud radiative effects. Merlis et al. (2012) address this by prescribing a cloud field to the radiation code (thereby including cloud radiative effects in their experiments); in contrast in our case, for simplicity, we do not prescribe any cloud radiative effects.

The new radiative transfer setup uses a diurnally varying solar forcing pattern, which is computed based on the specified obliquity and eccentricity of the orbit. This is in contrast to the initial version of the model, where the solar forcing was not subject to a diurnal cycle and was prescribed as a constant function of latitude (Frierson et al. 2006). To simplify the analysis, we run our control simulations with zero obliquity and eccentricity to remove any seasonal cycle in solar insolation; however we acknowledge that when running in this "perpetual equinox" mode, the annual average solar insolation at a given latitude in our simulations does not match the annual average solar insolation on Earth. The mixing ratios of the most significant well-mixed greenhouse gases, carbon dioxide, methane, and nitrous oxide are prescribed to present-day values ($CO_2 = 369.4$ ppm,

$CH_4 = 1.82$ ppm, and $N_2O = 316$ ppb). Additionally a hemispherically-symmetrized latitudinally-varying vertical profile of ozone, the same used in the Aquaplanet Model Intercomparison Project (Blackburn et al. 2013), is prescribed to the radiation code.

We run four control simulations with the above-mentioned diurnally-varying hemispherically-symmetric solar insolation pattern. The first is a case with the default value of the convective relaxation time of 2 hours used in Frierson (2007). The remaining three use convective relaxation times of 4, 8, and 16 hours respectively. We discuss briefly the climatology of the control simulation with the default convective relaxation time in Section 3a.

b. Hemispherically Asymmetric Forcings

To study the role of the water vapor feedback in influencing ITCZ shifts, we must first have a way to shift the ITCZ off the equator. Typically, studies using idealized moist models coupled to a slab ocean shift the ITCZ by applying a hemispherically asymmetric ocean heat flux into the atmosphere (e.g. Kang et al. 2008, 2009; Seo et al. 2014; Bischoff and Schneider 2014, 2015). In this study, instead of applying an ocean heat flux, we choose to modify the incoming solar radiation; another study that took a similar approach was Yoshimori and Broccoli (2009).

Under perpetual equinox conditions, with zero eccentricity, and a solar constant of S_0, the unperturbed solar radiation flux incident at the TOA at $t = 0$ as a function of latitude (θ) and longitude (ϕ) is given by:

$$S_{\text{control}}(\theta, \phi) = \begin{cases} S_0 \cos(\theta) \sin(\phi) & 0 \leq \phi < \pi \\ 0 & \pi \leq \phi < 2\pi. \end{cases} \tag{1}$$

Because of the zonally-symmetric nature of our boundary conditions, for the purposes of this derivation, we can ignore the time-dependence when taking the zonal and time mean of the insolation (in the model a diurnal cycle exists). Therefore, the zonal and time mean insolation is given by:

$$\overline{S_{\text{control}}}(\theta) = \frac{1}{2\pi}\int_0^{\pi} S_0 \cos(\theta)\sin(\phi)\,\mathrm{d}\phi = \frac{S_0\cos(\theta)}{\pi}. \tag{2}$$

In our study, we introduce a perturbation by imposing a latitudinal dependence on S_0. Replacing S_0 in Equation 1 with $S_0'(\theta)$ of the form

$$S_0'(\theta) = S_0 + \frac{\pi\overline{\delta S}(\theta)}{\cos(\theta)}, \tag{3}$$

generates a perturbed annual and zonal mean pattern of solar insolation of:

$$\overline{S_{\text{perturbed}}}(\theta) = \overline{S_{\text{control}}}(\theta) + \overline{\delta S}(\theta). \tag{4}$$

In Equations 3 and 4, and throughout the rest of this paper, the overbars represent time and zonal averages. Imposing the annual mean perturbation in this way ensures that so long as $S_0'(\theta)$ is greater than zero at all gridpoints in the model, the solar insolation at any given time, latitude, and longitude will be consistently greater than or equal to zero.

The shape of the zonal and time mean perturbation $\overline{\delta S}$ that we use is a Gaussian in latitude:

$$\overline{\delta S}(\theta) = -\frac{M}{M_0}\exp\left[-\frac{(\theta-\theta_a)^2}{2\sigma^2}\right], \tag{5}$$

where M_0 is a normalization parameter that ensures the global area average change in annual mean incoming shortwave radiation is given by $-M$, a measure of the strength of the perturbation:

$$M_0 = \frac{\int_{-\pi/2}^{\pi/2}\exp\left[-\frac{(\theta-\theta_a)^2}{2\sigma^2}\right]\cos(\theta)\,\mathrm{d}\theta}{\int_{-\pi/2}^{\pi/2}\cos(\theta)\,\mathrm{d}\theta}. \tag{6}$$

The parameter θ_a is the central latitude of the applied perturbation in degrees, and the parameter σ controls the width of the perturbation.

In all our simulations we apply a negative perturbation to the incoming solar radiation centered only in the northern hemisphere. This induces an ITCZ shift southward. Our experimental setup differs again from some prior studies (e.g. Kang et al. 2008, 2009; Seo et al. 2014; Bischoff and

Schneider 2014, 2015) in that the perturbation we apply is not antisymmetric. By "antisymmetric," we mean the perturbation in one hemisphere is matched by an equal and opposite perturbation in the other hemisphere. In our case, rather, the negative perturbation in the northern hemisphere is left unbalanced (as was done in Yoshimori and Broccoli (2009) and Ceppi et al. (2013)). This complicates analysis somewhat, because it changes the global mean surface temperature and column water vapor; however it more closely mimics the potential shortwave forcing imposed by heterogeneous variations in aerosols or clouds.

c. Perturbation Simulations

We are interested in the change in sensitivity of the ITCZ position to hemispherically asymmetric forcings with the inclusion of interactive water vapor and radiation versus without. To test this sensitivity, we apply the hemispherically asymmetric forcing described in Section 2b with varying magnitude (M) and location (θ_a) in two model configurations. The first is the default configuration of the idealized moist model with full radiative transfer, which includes the water vapor feedback; we refer to this as the "interactive" water configuration. The second configuration is the idealized moist model with full radiative transfer, but with the water vapor field seen by the radiation code prescribed as a symmetrized (i.e. the value at a given latitude is the average of the values at that latitude in the northern and southern hemispheres in the unsymmetrized case), zonal mean climatological water vapor field from a control simulation with hemispherically symmetric solar insolation; we refer to this as the "prescribed" water configuration.

We run all experiments with a surface albedo of 0.2725 to obtain a global mean surface temperature that approximates that of the Earth in the control simulation with symmetric solar insolation with a solar constant of $S_0 = 1365\,\mathrm{W m^{-2}}$. All experiments are run for six years, with the first two allowed for spinup and equilibration and the final four years used for analysis. All experiments are run with 30 vertical levels and at T42 spectral resolution (64 latitude by 128 longitude gridpoints).

In our experiments we vary the strength of the solar insolation perturbation, M, between 5, 10, 15, and 18 $\mathrm{W m^{-2}}$ and impose the change in the tropics ($\theta_a = 15°$N, and $\sigma = 4.94°$) and extratropics ($\theta_a = 60°$N, and $\sigma = 9.89°$) (Fig. 1). The parameter σ in each case is chosen such that the full width at 1/100th maximum is about 30° for a perturbation in the tropics and 60° for a perturbation in the extratropics. As we alluded to in Section 2b, to maintain a positive solar insolation at all latitudes given the latitudes of our gridpoints, we must take care in the magnitude of the perturbation we apply. For the Gaussian-shaped perturbation we apply in the extratropics, and our grid resolution, the maximum negative perturbation we can apply has a magnitude $M = 18\,\mathrm{W\,m^{-2}}$.

To test the sensitivity of water vapor's role in influencing the response of the ITCZ to hemispherically asymmetric perturbations to changes in the convection scheme used, we run analogous experiments with convective relaxation times of 4, 8, and 16 hours. In these cases the water vapor fields seen by the radiation code in the prescribed water configuration come from the hemispherically-symmetric control simulations with matching convective relaxation times.

3. Climatology of the idealized moist model with full radiative transfer

Given that we are using a new model configuration, we will begin by describing the climatological tropical circulation in the control case with hemispherically-symmetric solar insolation and the default convective relaxation time. We will then discuss the full radiation model's response to hemispherically-asymmetric perturbations to the solar insolation as described in Section 2, with an emphasis on the role of water vapor-radiation interaction in controlling the sensitivity of the ITCZ position to a given asymmetry.

a. Climatological Tropical Circulation

1) Net column heating

The net column heating is a useful diagnostic for investigating the energy budget of the atmosphere (Neelin and Held 1987); importantly, it can be used to compute the total vertically-integrated moist static energy flux, the zero of which has been shown to be correlated with the latitude of the ITCZ (Kang et al. 2008). Since we allow the model to run to equilibrium and run with zero ocean heat flux in all of our simulations, in the time and zonal mean, the net column heating reduces to simply the net top of atmosphere radiation:

$$\overline{Q} = \overline{S} - \overline{L}. \tag{7}$$

In the above equation, $\overline{Q}$ is the net column heating, while $\overline{S}$ is the net shortwave radiation at the top of the atmosphere and $\overline{L}$ is the outgoing longwave radiation (Bischoff and Schneider 2014).

In the control climate, the accumulation of water vapor in the vicinity of the ITCZ has a strong impact on the radiative budget. This is manifested by a pronounced peak in the net column heating in the deep tropics, with values rising sharply between 10° and 20° latitude from below 25 $\mathrm{W\,m^{-2}}$ to near 50 $\mathrm{W\,m^{-2}}$ at the equator [Figure 2(a)]. This peak exists for two primary reasons. The first is that there is a maximum in the zonal and time mean net shortwave radiation at the top of the atmosphere at the equator, associated simply with the geometry of the problem (perpetual equinox conditions and the angle of incidence of solar radiation on the surface) [Figure 2(a), dashed line]. The second is that the circulation and thermodynamically-induced distiribution of water vapor in the tropics leads to a local minimum in outgoing longwave radiation at the ITCZ [Figure 2(a), dashed-dotted line]. Panels (b) and (c) of Figure 2 illustrate how this occurs.

In Figure 2(b) we can see that, consistent with weak temperature gradient theory (Sobel et al. 2001), the meridional gradient in temperature throughout the tropical troposphere is near zero.

Therefore, the spatial structure we see in outgoing longwave radiation must result primarily from the spatial structure in longwave absorbers in the atmosphere (water vapor). Due to the nature of the circulation, with moist air rising at the ITCZ, and dry air subsiding in the subtropics, the relative humidity at the ITCZ is relatively high (around 0.7) and is relatively low in the subtropics (around 0.3). This, coupled with the weak temperature gradient, indicates a strong gradient in specific humidity between the deep tropics and subtropics. Specific humidity in the upper troposphere reaches a maximum in the deep tropics, inhibiting air from cooling to space through outgoing longwave radiation (i.e. for a given vertical profile of temperature there will be less outgoing longwave radiation in the deep tropics than in the subtropics); this results in a local minimum in outgoing longwave radiation in the deep tropics.

In our study, we design experiments which focus on the role of water vapor-radiation interaction in setting the sensitivity of the ITCZ latitude to a given hemispherically asymmetric forcing. While we do perturb the solar insolation in our experiments to shift the ITCZ, the maximum always remains at the equator. When the ITCZ shifts off the equator, the peak in mid-tropospheric relative humidity can shift along with it, altering the spatial distribution of net column heating.

2) ITCZ in control simulation

The strong peak in net column heating in the deep tropics is associated with net divergence of moist static energy. In this model this is achieved primarily through transient eddy fluxes of dry static energy, even near the equator [Figure 3(a)]. A component of the moist static energy flux is the moisture flux; unlike the total moist static energy, moisture is converged at the ITCZ primarily through the mean circulation, leading to a narrow peak in precipitation minus evaporation [Figure 3(b)]. The spatial structure in precipitation minus evaporation is primarily determined by the narrowness of the ascending branch of the Hadley circulation [Figure 3(c)], which carries moist air upward leading to precipitation.

With a global mean surface temperature of 284.5 K, the precipitation rate at the ITCZ is around $10\,\mathrm{mm\,d^{-1}}$. In addition, the strength of the streamfunction reaches around $10 \times 10^{10}\,\mathrm{kg\,s^{-1}}$.

4. Sensitivity of ITCZ latitude to hemispherically asymmetric perturbations

a. ITCZ position in cases with default convective relaxation time

Our primary experiments are designed with the aim of understanding the role of feedbacks between water vapor, radiation, and the circulation in setting the sensitivity of the ITCZ position to hemispherically asymmetric perturbations. As in Seo et al. (2014) and Bischoff and Schneider (2014, 2015) we define the position of the ITCZ as the latitude of the maximum zonal mean precipitation rate. To compute this latitudinal position at a sub-gridscale level, we use cubic interpolation to infer the zonal annual mean precipitation rate at a resolution of 0.01 degrees latitude and then select the latitude where the precipitation rate maximizes. In cases with the default convective relaxation time (as discussed in this section), the precipitation rate is the sum of the large scale and convective precipitation rates. Figure 4 shows a sample precipitation profile with the ITCZ shifted off the equator from a case with interactive water vapor and radiation and a $M = 15\,\mathrm{Wm^{-2}}$ perturbation imposed in the tropics. The ITCZ latitude as computed using the method described is plotted as the dashed black line. The maximum of the column integrated water vapor follows the ITCZ.

1) Sensitivity to perturbation asymmetry and location

In Figure 5 we show the latitude of the ITCZ plotted against the hemispheric asymmetry in net solar radiation in cases with interactive (closed symbols) and prescribed water vapor (open symbols). We define the hemispheric asymmetry of a quantity $(\cdot)$, $A(\cdot)$, as the area-weighted average of the quantity in the northern hemisphere minus the average of the in the southern hemisphere:

$$A(\cdot) = \{\cdot\}_{\mathrm{NH}} - \{\cdot\}_{\mathrm{SH}}. \tag{8}$$

In Equation 8 the braces represent area-weighted averages of $(\cdot)$ over the subscript region. Here the hemispheric asymmetry in net solar radiation plotted is $(1-\alpha)A(\overline{S})$, where α is the surface albedo, and $\overline{S}$ is the zonal and time mean solar insolation. Note that in this calculation we are ignoring the effects of water vapor shortwave absorption.

Within the range of perturbation asymmetries tested, the ITCZ always shifts more as the magnitude of the hemispheric asymmetry is increased. In addition, the ITCZ shift is more sensitive to a perturbation imposed in the tropics [Figure 5(a)] than that in the extratropics [Figure 5(b)]. For example, the ITCZ shifts most off the equator in response to the $M = 18\,\mathrm{Wm}^{-2}$ perturbation imposed in the tropics with interactive water vapor interaction, shifting to a latitude of 9.17°S, while the same magnitude perturbation imposed in the extratropics results in a shift to 2.03°S in the interactive water configuration. Finally, the ITCZ is more sensitive in cases with interactive water vapor and radiation than with prescribed water vapor, with the open symbols (representing the ITCZ latitude in cases with prescribed water) in Figures 5(a) and 5(b) always falling equatorward of the closed symbols (representing the ITCZ latitude in cases with interactive water) for equivalent forcings.

2) Diagnostic theories for the ITCZ latitude

It is possible to investigate the difference in sensitivity of the ITCZ latitude to a given perturbation between cases with interactive water and cases with prescribed water using several theories that provide diagnostic estimates of the latitude of the zonal-mean-precipitation-maximum defined ITCZ in terms of other climate variables. These theories are classified into two categories by Shekhar and Boos (2016): (1) convective quasi-equilibrium-based theories, and (2) moist static energy budget-based theories.

Theories for the ITCZ latitude based on convective quasi-equilibrium suggest that the ITCZ is collocated with the sub-cloud layer moist static energy maximum (e.g. Emanuel 1995; Privé and Plumb 2007; Shekhar and Boos 2016). In an aquaplanet setting, because the boundary layer is typically saturated everywhere (meaning the sub-cloud layer specific humidity can be approximated as a function of temperature), this approximately reduces to the statement that the ITCZ is collocated with the latitude of maximum zonal-mean surface temperature (Voigt et al. 2013). While this tends to be a fairly accurate diagnostic theory in our experiments, it is difficult to relate the latitude of maximum surface temperature directly to changes in the radiative properties of the atmosphere. In addition this diagnostic can break down when meridional gradients of sub-cloud MSE near its maximum are weak (i.e. the maximum is fairly broad and flat), for example in the CREonSW and CREoff experiments of Popp and Silvers (2017).

Energy flux equator theory states that the ITCZ is approximately coincident with the zero of the total vertically integrated moist static energy flux (Kang et al. 2008). The vertically intergrated moist static energy flux can be related to the net column heating (Neelin and Held 1987; Hill et al. 2014), which in our case in the time mean at equilibrium (using a slab ocean with zero prescribed ocean heat flux) is just the net top of atmosphere radiation at a given latitude (Equation 7). Through the moist static energy budget and energy flux equator theory, the net column heating provides a theoretical link between the latitude of the ITCZ and the TOA radiative fluxes. Since our experiments are based on differences in the treatment of atmospheric radiative transfer, this is a useful framework for the discussion of our results.

3) Applicability of energy flux equator theory

Before proceeding, to assess the applicability of energy flux equator theory in our experiments, we plot the latitude of the energy flux equator versus the ITCZ latitude (Figure 6) for all cases with the default convective relaxation time. We compute the latitude of the energy flux equator by first computing the vertically integrated meridional moist static energy flux following Hill et al. (2014) and then, as we did in finding the latitude of the ITCZ, use cubic interpolation to sharpen the resolution to find the latitude of zero flux to within 0.01 degrees. Since all the points in Figure 6 are above the one-to-one line, the energy flux equator in general overestimates the shift in ITCZ for cases with the default convective relaxation time. The points form a line that is roughly linear and passes through the origin. If we apply least squares regression, we obtain the following relationship:

$$\theta_{\mathrm{ITCZ}} \approx 0.64\,\theta_{\mathrm{EFE}}. \tag{9}$$

The fitted line has a coefficient of determination of 0.95. Therefore differences in the latitude of the energy flux equator between cases with the default convective relaxation time can be approximately related to differences in the latitude of the ITCZ by a scaling factor of 0.64. Therefore despite the importance of the eddy moist static energy flux in this model (Figure 2), which in theory could weaken the correspondence of the ITCZ latitude to the zero of the total moist static energy flux (Kang et al. 2008; Bischoff and Schneider 2015), the two remain correlated. Given this result, we will proceed in linking the energy flux equator position to the net column heating.

4) Linking the latitude of the energy flux equator to the net column heating

Building on the results in Kang et al. (2008), studies have linked the off-equatorial ITCZ position with the cross-equatorial moist static energy flux (Frierson and Hwang 2011; Donohoe et al. 2013; Voigt et al. 2013). Assuming this flux is approximately linear with latitude near the equator and using the moist static energy budget, Bischoff and Schneider (2014) show that one can derive a relationship between the cross equatorial energy flux and equatorial net column heating, and the energy flux equator latitude (in radians):

$$\theta_{EFE} \approx -\frac{1}{2\pi a^2}\frac{\overline{F_0}}{\overline{Q_0}}. \tag{10}$$

In Equation 10, $\overline{F}$ is the vertically integrated moist static energy flux, $\overline{Q}$ is the net column heating as defined in Equation 7, and a is the radius of the Earth; the subscript 0's indicate that each are evaluated at the equator. In our experiments, the approximation in Equation 10 holds well. If we plot the result of this approximation (noting to convert from radians to degrees), the points follow the one-to-one line closely (Figure 7); a line of best fit through the origin has a slope of 0.98 and a coefficient of determination of 0.98. This suggests that in our discussion of differences in the latitude of the energy flux equator, and by extension the ITCZ, we can focus on differences in the cross equatorial energy flux or equatorial net column heating.

Through the moist static energy budget, one can exactly relate the cross equatorial energy flux to the hemispheric asymmetry in net column heating (Frierson and Hwang 2011; Voigt et al. 2013):

$$\overline{F_0} = -\pi a^2 A(\overline{Q}). \tag{11}$$

Here A is the hemispheric asymmetry operator as defined in Equation 8. If the area average net column heating of the northern hemisphere is greater than that in the southern hemisphere, there must be a cross equatorial energy flux out of the northern hemisphere into the southern hemisphere (hence the negative sign) as the global time mean column heating is zero. By combining Equation 10 with Equation 11, we can therefore approximate the latitude of the energy flux equator through knowledge of the net column heating alone:

$$\theta_{EFE} \approx \frac{A(\overline{Q})}{2\overline{Q_0}}. \tag{12}$$

As such, the energy flux equator's displacement from the geographic equator approximately depends on the magnitude of the hemispheric asymmetry in net column heating (the numerator in Equation 12), and the equatorial net column heating (the denominator).

5) Differences between cases with interactive and prescribed water vapor

The ITCZ shifts approximately twice as much for a given perturbation with interactive water vapor and radiation than with prescribed water vapor-radiation interaction (Figure 8). Equation 12 shows that there is an approximate positive relationship between the hemispheric asymmetry in net column heating and the latitude of the energy flux equator (and by extension the ITCZ). Previous studies (e.g. Frierson and Hwang 2011; Donohoe et al. 2013; Voigt et al. 2013) have leveraged this relationship to understand ITCZ shifts within the context of changes to the hemispheric asymmetry in net column heating, under the implicit assumption that the equatorial net column heating remains roughly constant across experiments. To be thorough, we will consider the possibility of both differences in the hemispheric asymmetry in net column heating and differences in the equatorial net column heating in contributing to changes in the energy flux equator position between cases.

Using the approximation in Equation 12, we can decompose a change in the latitude of the energy flux equator into components due to differences in the hemispheric asymmetry in net column heating and differences in the net column heating at the geographic equator:

$$\delta\theta_{EFE} \approx \frac{1}{2\overline{Q_0}}\delta A(\overline{Q}) - \frac{A(\overline{Q})}{2\overline{Q_0}^2}\delta\overline{Q_0}. \tag{13}$$

Figure 9 shows the results of this decomposition. We can see that the approximation holds well; the sum of the components (black circles) align fairly closely to the one-to-one line. We find that it is differences in the hemispheric asymmetry in net column heating that dominate the difference in energy flux equator position. Differences in equatorial net column heating play a lesser role, particularly when the perturbation is imposed in the extratropics. As mentioned before, the correspondence between differences in the energy flux equator latitude and differences in the precipitation maximum-defined ITCZ is not as strong, however, particularly for large perturbations.

Given that interactive water vapor and radiation tends to amplify the displacement of the energy flux equator from the geographic equator for a given perturbation (Figure 8), and that this amplification is primarily due to an increase in the hemispheric asymmetry in net column heating (Figure 9), we can investigate water vapor's role in amplifying the hemispheric asymmetry in net column heating. To begin this discussion, we will note that the hemispheric asymmetry, defined in Equation 8 as the difference in area-weighted averages of a quantity between the hemispheres, can equivalently be expressed in integral form (Frierson and Hwang 2011). For example, the hemispheric asymmetry in net column heating can be can be expressed as:

$$A(\overline{Q}) = \int_0^{\pi/2} \left[\overline{Q}(\theta) - \overline{Q}(-\theta)\right] \cos\theta \, \mathrm{d}\theta. \tag{14}$$

In this sense, the asymmetry is the area-weighted average of the difference between the net column heating at a latitude in the northern hemisphere and the net column heating at the same latitude in the southern hemisphere (from here on we will refer to this integrand as the "point-wise asymmetry"). We will abbreviate the mathematical form of the point-wise asymmetry of a quantity $\overline{f}$ as:

$$P(\overline{f}) = \overline{f}(\theta) - \overline{f}(-\theta). \tag{15}$$

By computing the difference in the point-wise asymmetry between two simulations we can gain insight into which locations are most responsible for the difference in their total hemispheric asymmetry.

Figures 10(a) and 10(b) show the difference in point-wise asymmetry in net column heating between cases with interactive and prescribed water with a $M = 15\,\mathrm{Wm}^{-2}$ perturbation imposed in the tropics or extratropics respectively. Building off Frierson and Hwang (2011) and Voigt et al. (2013), we can decompose a difference in point-wise asymmetry in net column heating into components due to that in net shortwave or outgoing longwave radiation at TOA:

$$\delta P(\overline{Q}) = \delta P(\overline{S}) - \delta P(\overline{L}). \tag{16}$$

It is clear that the difference in point-wise asymmetry for both perturbation locations is due primarily to differences in longwave asymmetry. The difference in longwave asymmetry in the tropics is collocated with a large difference in asymmetry in column integrated water vapor (Figures 10c and 10d). This supports the notion first put forth in Yoshimori and Broccoli (2009) and Frierson and Hwang (2011) that the water vapor content associated with the ITCZ acts as a positive feedback, amplifying the ITCZ's shift in response ot a given perturbation; this is because a southward ITCZ shift makes the total hemispheric asymmetry in net column heating more negative, shifting the ITCZ farther south.

The difference in longwave point-wise asymmetry in the tropics is a dominant component of the difference in total hemispheric asymmetry for all perturbation magnitudes and locations. Recall that the total difference in the hemispheric asymmetry in net column heating is the area average of the difference in point-wise asymmetry. We can decompose that area average into components over the tropics (0° to 30°N) and extratropics (30°N to 90°N). The results are tabulated in Table 1; percentages of the overall hemispheric difference are in parentheses. In cases with the perturbation imposed in the tropics, the difference in longwave asymmetry in the tropics accounts for around 80% of the total difference. The difference in shortwave asymmetry in the tropics approximately accounts for the rest. The two components roughly cancel each other out in the extratropics, with shortwave asymmetries acting to slightly amplify the total asymmetry, but longwave asymmetries acting to slightly dampen it out.

When the perturbation is imposed in the extratropics, the difference in longwave asymmetry in the tropics remains important, providing the most significant amplifying component (69% to 101%) to the total hemispheric asymmetry (Table 1). In contrast, it becomes an appreciable dampening factor in the extratropics (-22% to -63%). The shortwave asymmetries in the tropics and extratropics act to offset this damping component.

6) Physical mechanisms

Since water vapor is simultaneously an absorber of both shortwave and longwave radiation, differences in the treatment of water vapor-radiation interaction lead to the differences in the net column heating asymmetry between the interactive and prescribed water cases. With interactive water vapor and radiation, the radiation code sees a water vapor field that is always consistent with the temperature and circulation of the atmosphere; with prescribed water vapor-radiation interaction, the radiation code sees a constant water vapor field, that does not respond to changes in temperature or circulation.

In the context of net shortwave radiation at TOA, this means that in the prescribed water cases, any asymmetry in shortwave radiation is due only to the imposed perturbation, since the planetary albedo in the prescribed water case does not change. Therefore when the perturbation is imposed in the tropics (extratropics) there is zero shortwave asymmetry in the extratropics (tropics), in cases with prescribed water (not shown). In cases with interactive water vapor and radiation, the planetary albedo is allowed to change. Since we are imposing negative perturbations, which induce cooling, the specific humidity decreases in the vicinity of the perturbations, which is accompanied by a subsequent decrease in absorbed solar radiation (not shown). This decrease in absorbed shortwave radiation occurs primarily in the northern hemisphere (where we impose the perturbation);

therefore it tends to mildy enhance the total hemispheric asymmetry in net column heating with respect to a prescribed water case with the same perturbation.

In the context of outgoing longwave radiation, prescribed water vapor-radiation interaction means that changes are due only to changes in temperature. In the tropics, temperature is fairly uniform (Sobel et al. 2001). Therefore any cooling that takes place happens with only a minor hemispheric asymmetry, leading to minor tropical asymmetries in outgoing longwave radiation. With interactive water vapor and radiation, however, the latitudinal pattern of the longwave optical depth of the atmosphere changes significantly as the ITCZ moves. The ITCZ is a local maximum in the atmospheric longwave optical depth, because of high specific humidities in its vicinity and lower specific humidities in the subsidence regions surrounding it (Pierrehumbert 1995). This acts to decrease outgoing longwave radiation in the vicinity of the ITCZ, which has a tendency to increase net column heating. Since the ITCZ shifts into the hemisphere with greater net column heating (a moistening influence) and away from the hemisphere with smaller net column heating (a drying influence), this is a positive feedback, leading to an amplification of the shift to a given perturbation. This mechanism is the most important distinguishing factor between the interactive and prescribed water cases.

In addition to the positive feedbacks discussed above, a negative feedback appears to exist in the extratropics, regardless of the location of the forcing, damping the asymmetry in the interactive water vapor case relative to the prescribed water vapor case. This is evidenced by the positive contribution of longwave radiation to the difference in hemispheric asymmetry between the interactive and prescribed water vapor cases poleward of about 50° latitude in Figures 10(a) and (b). The difference between the interactive and prescribed water vapor cases is dominated by the difference in the northern hemisphere (the hemisphere in which we apply the forcing); there is less outgoing longwave radiation in the northern hemisphere extratropics in the interactive water vapor case than in the prescribed water vapor case (not shown), consistent with reduced atmospheric moist static energy flux convergence.

It has been shown in multiple studies that, consistent with poleward amplification of warming (cooling), poleward moist static energy transport increases (decreases) under an imposed positive (negative) forcing (Hwang and Frierson 2010; Frierson and Hwang 2011; Ocko et al. 2014). More specifically, there is evidence that the water vapor feedback plays a role in strengthening this behavior; for example Langen et al. (2012) show in a hemispherically-symmetric aquaplanet model that including the water vapor feedback under a doubling of carbon dioxide increases poleward moist static energy transport and moist static energy convergence in the extratropics, permitting enhanced outgoing longwave radiation and warmer temperatures. In our simulations, we see the converse; we apply a localized cooling forcing in the northern hemisphere. In the simulations with the water vapor feedback, we have reduced moist static energy convergence in the northern hemisphere extratropics relative to the simulations without the water vapor feedback. In this manner one can think of the positive contribution of the difference in pointwise asymmetry in outgoing longwave radiation to the difference in pointwise asymmetry in net column heating in the extratropics [illustrated in Figures 10(a) and (b)] as a manifestation of the water vapor feedback's role in the polar amplification of the imposed cooling in the northern hemisphere.

b. Sensitivity to increases in the convective relaxation time

In a previous study, using a variant of our model, variation of the convective relaxation time was shown to alter the relative humidity distribution in the tropics, in particular the contrast in relative humidity between the ITCZ and subtropics (Frierson 2007). Our results suggest that this contrast may be important for setting the sensitivity of the ITCZ latitude to a given hemispherically-asymmetric forcing; therefore it is possible that changing this contrast (through changing the convective relaxation time) could alter the magnitude of an ITCZ shift to a given forcing. Here we discuss the results of experiments described above repeated using convective relaxation times of 4, 8, and 16 hours, and how they differ from the results using a convective relaxation time of 2 hours.

1) Sensitivity to perturbation asymmetry and location

As we increase the convective relaxation time the ITCZ tends to shift more for a given forcing with interactive water vapor and radiation (filled symbols in Figure 11). This is particularly evident for strong forcings imposed in the tropics, where the ITCZ shifts to 12.9°S with a forcing asymmetry of $-26.1\,\mathrm{W\,m^{-2}}$ and convective relaxation time of 16 h, but only shifts to 9.1°S for the same forcing asymmetry but a convective relaxation time of 2 h. In contrast, with prescribed water vapor-radiation interaction, the magnitude of the shift in the ITCZ for a given forcing is relatively insensitive to the convective relaxation time (open symbols in Figure 11).

For all convective relaxation times tested in our experiments, the ITCZ always shifts more with interactive water vapor and radiation than with prescribed. The scale factor relating the ITCZ latitude in the interactive water vapor experiments to the ITCZ latitude in prescribed water experiments increases as the convective relaxation time increases from 2.0 with $\tau_{\mathrm{SBM}} = 2\,\mathrm{h}$ to 2.76 with $\tau_{\mathrm{SBM}} = 16\,\mathrm{h}$ (Figure 12).

2) Relative importance of changes in cross-equatorial MSE flux and equatorial net column heating

With increased convective relaxation time, the energy flux equator continues to shift more for a given forcing and model configuration than the precipitation-maximum-defined ITCZ. Again linear scaling relationships still approximately hold to relate the two for a given convective relaxation time. As in the case with the default convective relaxation time, these linear scalings break down as the ITCZ moves significantly off the equator (in particular for the two strongest forcings imposed in the tropics); however, they remain useful for the weaker tropical forcings, and all the extratropical forcings.

Figure 13 plots the ITCZ latitude versus the energy flux equator latitude for the case with $\tau_{\mathrm{SBM}} = 16\,\mathrm{h}$; plots for $\tau_{\mathrm{SBM}} = 4\,\mathrm{h}$ or $\tau_{\mathrm{SBM}} = 8\,\mathrm{h}$ look similar, only having slightly different scaling relationships (slopes of 0.68 and 0.74 respectively, compared with 0.84 for $\tau_{\mathrm{SBM}} = 16\,\mathrm{h}$). With these quantitative relationships between the ITCZ latitude and the energy flux equator for each τ_{SBM} we can apply the same systematic analysis we applied to the cases the the default convective relaxation time.

As found for the case with the default convective relaxation time, the difference in energy flux equator latitude between the interactive and prescribed water vapor cases can be explained predominantly by a difference in the cross-equatorial moist static energy flux for simulations with convective relaxation times of 4, 8, or 16 hours. Figure 14 shows the decomposition, defined in Equation 13, for the simulations with $\tau_{\mathrm{SBM}} = 16\,\mathrm{h}$, indicating that the cross equatorial energy flux components (the red triangles) make up most of the difference in the energy flux equator positions (the dashed line) between the interactive and prescribed water vapor cases. Results for convective relaxation times of 4 and 8 hours look similar.

3) Role of water vapor

Finally, the differences in the cross-equatorial moist static energy flux are again primarily the result of differences in the pointwise asymmetry in net column heating in the tropics for all convective relaxation times tested. Figure 15 shows the difference in pointwise asymmetry between the interactive and prescribed water vapor cases for $\tau_{\mathrm{SBM}} = 16\,\mathrm{h}$ and $M = 15\,\mathrm{W\,m^{-2}}$. As before, this difference is driven mostly by the shift in longwave radiation absorption by water vapor associated with the ITCZ. We see similar behavior for the cases with convective relaxation times of 4 and 8 hours, which suggests that this physical mechanism is dominant across changes to this model's convection scheme.

4) Increase in the scale factor relating the ITCZ latitude in the interactive WV cases and the prescribed WV cases

In Section 4b.1 we note that as we increase the convective relaxation time, the scale factor relating the ITCZ latitude in the interactive water vapor and prescribed water vapor cases increases. Qualitatively, this can be explained by an increase in the contrast in net column heating between the ITCZ and the subtropics as the convective relaxation time increases. In symmetric control simulations, as we increase the convective relaxation time, the relative humidity throughout troposphere at the ITCZ increases, but there is little change in the relative humidity in the subtropics (Figure 16). This increases longwave radiation absorption in the vicinity of the ITCZ, thereby on average increasing the net column heating in the region 20°S to 20°N from 38.8 $\mathrm{W\,m^{-2}}$ in the $\tau_{\mathrm{SBM}} = 2\,\mathrm{h}$ case to 39.0, 39.4, and 39.6 $\mathrm{W\,m^{-2}}$ in the $\tau_{\mathrm{SBM}} = 4$, 8, and 16 h cases respectively. In addition, the average net column heating in the subtropics 30°S to 20°S and 20°N to 30°N decreases from 19.5 $\mathrm{W\,m^{-2}}$ in the $\tau_{\mathrm{SBM}} = 2\,\mathrm{h}$ case to 19.0, 18.7, and 19.0 $\mathrm{W\,m^{-2}}$ in the $\tau_{\mathrm{SBM}} = 4$, 8, and 16 h cases respectively (Figure 17). If the net column heating in the vicinity of the ITCZ increases and the net column heating in the subtropics decreases, the additional asymmetry the ITCZ induces per degree shift in the cases with interactive water vapor and radiation increases. This could strengthen the positive feedback that forms the basis of the difference between the interactive and prescribed water vapor cases (described in Section 4a.6). Because of the strengthened feedback, the ITCZ shifts more. Another possibility could be that the strength of the negative feedback in the extratropics, related to weakened atmospheric heat transport in the high-latitudes of the northern hemisphere in cases with the water vapor feedback, is reduced in the cases with greater convective relaxation time.

It is important to note that while in the spatial average this mechanism looks clear, if we look at the fine details of the difference in net column heating between the control simulations with varying τ_{SBM} and the simulation with the default τ_{SBM} we can see that the behavior is not monotonic at all latitudes. For instance between 10° and 20°, there is little difference in the net column heating between the $\tau_{\mathrm{SBM}} = 16\,\mathrm{h}$ and the $\tau_{\mathrm{SBM}} = 2\,\mathrm{h}$ cases, but there is a positive difference for the $\tau_{\mathrm{SBM}} = 4\,\mathrm{h}$ case, and a larger positive difference for the $\tau_{\mathrm{SBM}} = 8\,\mathrm{h}$ case. There is also a greater decrease in net column heating in the subtropics (between 20° and 30°) for the $\tau_{\mathrm{SBM}} = 8\,\mathrm{h}$ than for the $\tau_{\mathrm{SBM}} = 4\,\mathrm{h}$ or $\tau_{\mathrm{SBM}} = 16\,\mathrm{h}$ cases. This suggests that the response of the model to changing the convective relaxation time may be more complex than the average numbers make it appear.

5. Discussion

Previous studies have suggested that the water vapor feedback could play a role in amplifying the response of the ITCZ to a given hemispherically asymmetric forcing. Kang et al. (2009) show that compensation (i.e. the extent to which the cross equatorial energy flux compensates for the imposed hemispheric asymmetry) decreases when they prescribe the water vapor distribution seen by the radiation code in an aquaplanet comprehensive GCM. They argue that this is because the water vapor feedback acts locally to amplify the given forcing. Here we show that in an idealized model without clouds that local amplification of the extratropical forcing is a secondary effect (as evidenced by the partially offsetting contributions of differences in shortwave and longwave radiation asymmetries in the extratropics to the total difference in hemispheric asymmetry in net column heating in Table 1); from the perspective of the net column heating, the local decrease in shortwave absorption in the vicinity of the forcing is mostly balanced, or exceeded, by a local decrease in temperature and decrease in outgoing longwave radiation. The amplification effect associated with water vapor-radiation interaction in our experiments is mainly due to the shift of the water vapor-rich ITCZ into the hemisphere with greater net column heating, consistent with the conclusions of Yoshimori and Broccoli (2009) and Frierson and Hwang (2011). This is true regardless of whether the forcing is imposed in the tropics or extratropics.

What does differ between the tropical and extratropical cases is extent of the ITCZ shift in response to a given magnitude forcing. For all model configurations tested (interactive versus prescribed water vapor, varying convective relaxation times), a forcing imposed in the tropics always results in a larger ITCZ shift than an equivalent-magnitude forcing in the extratropics. In this sense, the behavior is similar to that seen in Seo et al. (2014) in a similar idealized moist model configured with gray radiative transfer (i.e. no water vapor feedback). This is in contrast to what was observed in a comprehensive aquaplanet GCM, where the shortwave cloud feedback, strongest in the extratropics, provided an additional amplifying mechanism to enhance the hemispheric asymmetry in net column heating, ultimately leading to an extratropical forcing being more effective than a tropical one (Seo et al. 2014). This difference in behavior between idealized and comprehensive models underscores the importance of understanding all feedbacks in the climate system with respect to the sensitivity of the ITCZ latitude to hemispherically symmetric forcings.

When we vary the convective relaxation time, in effect altering activity of the convection scheme in the model, the ITCZ still moves more in response to a given forcing with interactive water vapor and radiation than with prescribed. However, while the physical mechanism responsible for the increased sensitivity of the ITCZ latitude to a given forcing in the interactive water vapor cases when compared with the prescribed water vapor cases remains the same for all values of τ_{SBM} tested, the quantitative value of the increase in sensitivity changes (increasing with increasing τ_{SBM}). This is empirical evidence that changes to the convection scheme used could impact the quantitative difference in sensitivity between the interactive and prescribed water vapor cases (i.e. with and without water vapor feedback). Lastly, an important caveat is that the sensitivity experiments described here (limited to changing the convective relaxation time) do not rule out that more extreme changes to the convection scheme used in the model (e.g. turning it off entirely or switching to a different type) could alter even the qualtitative differences between cases with interactive and prescribed water vapor.

It has been noted in prior studies that even in setups with minimal radiative feedbacks (e.g. with locked clouds (Voigt et al. 2013) or in an idealized moist model with gray radiation (Kang et al. 2009)) that the sensitivity of the ITCZ latitude to a given hemispherically asymmetric forcing can change as a result of changing the convection scheme alone. Here we find that in cases with prescribed water vapor (i.e. without the water vapor feedback) that the sensitivity of the ITCZ latitude to a given hemispherically asymmetric forcing is relatively invariant to the convective relaxation time used (see the open symbols in Figure 11); however, it again is possible that more extreme changes to the convection scheme could cause a change to the sensitivity of the ITCZ latitude in this model without the water vapor feedback.

The shift-amplification mechanism illustrated in this study, namely the movement of the anomalous net column heating associated with the ITCZ into the warmer hemisphere, has also been discussed within the context of the cloud radiative effect (CRE) (Voigt et al. 2013). The radiative effect of the clouds associated with the ITCZ depends on the their shortwave albedo (which acts as a cooling term in the net column heating) and their absorption of longwave radiation (which acts as a heating term, and is stronger for high clouds (Hartmann 2016)). Both of these opposing components depend on the physics and microphysics parameterizations used in a particular model. If they enhance the net column heating anomaly associated with water vapor's absorption of radiation in the vicinity of the ITCZ, then the ITCZ latitude would be more sensitive to hemispherically asymmetric forcings; if they dampen the net column heating anomaly, the ITCZ latitude will become less sensitive. Regardless, given the robustness of the increase in sensitivity associated with the interactive water experiments, we would expect the baseline sensitivity of the ITCZ latitude to hemispherically asymmetric forcings to be greater in comprehensive GCM's than in an idealized moist model with gray radiative transfer; how clouds alter the sensitivity from that baseline depends on how their effects are parameterized.

6. Conclusion

Our results reinforce the importance of understanding the net radiative effects of the water (both in the form of vapor and clouds) associated with the ITCZ in the atmosphere. As long as the contribution to the net column heating is net positive, then by energy flux equator theory, if the ITCZ were to move into a particular hemisphere, there would be a positive feedback leading it to move farther poleward. The sign of the net column heating perturbation associated with the ITCZ determines the sign of the feedback, and the magnitude of the net column heating perturbation determines the strength of the feedback. In the case of water vapor only, the net column heating perturbation associated with the ITCZ is net positive, leading to an amplification of an initial shift. With clouds, it has been shown that depending on the details of the moist convection parameterized and cloud scheme, the sign and magnitude net column heating perturbation associated with the ITCZ are less clear (Voigt et al. 2013).

Acknowledgments. We thank Spencer Hill for extensive discussions about the moist static energy budget and computational procedures, and Hailey Shin for guidance regarding the boundary layer scheme used in the model. We also thank Pu Lin and Nadir Jeevanjee for helpful comments on an earlier draft of this manuscript. S.K.C. was initially supported by the Cooperative Institute for Climate Science and later by a National Defense Science and Engineering Graduate Fellowship.

References

Bischoff, T., and T. Schneider, 2014: Energetic Constraints on the Position of the Intertropical Convergence Zone. *Journal of Climate*, **27 (13)**, 4937–4951, doi:10.1175/JCLI-D-13-00650.1.

Bischoff, T., and T. Schneider, 2015: The Equatorial Energy Balance, ITCZ Position, and Double-ITCZ Bifurcations. *Journal of Climate*, **29 (8)**, 2997–3013, doi:10.1175/JCLI-D-15-0328.1.

Blackburn, M., and Coauthors, 2013: The Aqua-Planet Experiment (APE): CONTROL SST Simulation. *Journal of the Meteorological Society of Japan. Ser. II*, **91A**, 17–56, doi:10.2151/jmsj.2013-A02.

Boucher, O., and Coauthors, 2013: Clouds and Aerosols. *Climate Change 2013: The Physical Science Basis. Contribution of Working Group I to the Fifth Assessment Report of the Intergovernmental Panel on Climate Change*, 571–657.

Ceppi, P., Y.-T. Hwang, X. Liu, D. M. W. Frierson, and D. L. Hartmann, 2013: The relationship between the ITCZ and the Southern Hemispheric eddy-driven jet. *Journal of Geophysical Research: Atmospheres*, **118 (11)**, 5136–5146, doi:10.1002/jgrd.50461.

Chiang, J. C. H., and C. M. Bitz, 2005: Influence of high latitude ice cover on the marine Intertropical Convergence Zone. *Climate Dynamics*, **25 (5)**, 477–496, doi:10.1007/s00382-005-0040-5.

Clark, S. K., D. S. Ward, and N. M. Mahowald, 2015: The sensitivity of global climate to the episodicity of fire aerosol emissions. *Journal of Geophysical Research: Atmospheres*, **120 (22)**, 2015JD024 068, doi:10.1002/2015JD024068.

Cvijanovic, I., and J. C. H. Chiang, 2012: Global energy budget changes to high latitude North Atlantic cooling and the tropical ITCZ response. *Climate Dynamics*, **40 (5-6)**, 1435–1452, doi: 10.1007/s00382-012-1482-1.

Cvijanovic, I., P. L. Langen, E. Kaas, and P. D. Ditlevsen, 2013: Southward Intertropical Convergence Zone Shifts and Implications for an Atmospheric Bipolar Seesaw. *Journal of Climate*, **26 (12)**, 4121–4137, doi:10.1175/JCLI-D-12-00279.1.

Donohoe, A., J. Marshall, D. Ferreira, and D. McGee, 2013: The Relationship between ITCZ Location and Cross-Equatorial Atmospheric Heat Transport: From the Seasonal Cycle to the Last Glacial Maximum. *Journal of Climate*, **26**, 3597–3618.

Dyer, A. J., 1974: A review of flux-profile relationships. *Boundary-Layer Meteorology*, **7 (3)**, 363–372, doi:10.1007/BF00240838.

Emanuel, K. A., 1995: The Behavior of a Simple Hurricane Model Using a Convective Scheme Based on Subcloud-Layer Entropy Equilibrium. *Journal of the Atmospheric Sciences*, **52 (22)**, 186–218.

Frierson, D. M. W., 2007: The Dynamics of Idealized Convection Schemes and Their Effect on the Zonally Averaged Tropical Circulation. *Journal of the Atmospheric Sciences*, **64 (6)**, 1959–1976, doi:10.1175/JAS3935.1.

Frierson, D. M. W., I. M. Held, and P. Zurita-Gotor, 2006: A Gray-Radiation Aquaplanet Moist GCM. Part I: Static Stability and Eddy Scale. *Journal of the Atmospheric Sciences*, **63 (10)**, 2548–2566, doi:10.1175/JAS3753.1.

Frierson, D. M. W., I. M. Held, and P. Zurita-Gotor, 2007: A Gray-Radiation Aquaplanet Moist GCM. Part II: Energy Transports in Altered Climates. *Journal of the Atmospheric Sciences*, **64 (5)**, 1680–1693, doi:10.1175/JAS3913.1.

Frierson, D. M. W., and Y.-T. Hwang, 2011: Extratropical Influence on ITCZ Shifts in Slab Ocean Simulations of Global Warming. *Journal of Climate*, **25 (2)**, 720–733, doi:10.1175/JCLI-D-11-00116.1.

Hartmann, D. L., 2016: Chapter 3 - Atmospheric Radiative Transfer and Climate. *Global Physical Climatology (Second Edition)*, Elsevier, Boston, 49–94.

Held, I. M., and B. J. Soden, 2000: Water vapor feedback and global warming. *Annu. Rev. Energ. Environ.*, **25**, 441–475.

Held, I. M., and B. J. Soden, 2006: Robust Responses of the Hydrological Cycle to Global Warming. *Journal of Climate*, **19 (21)**, 5686–5699, doi:10.1175/JCLI3990.1.

Hill, S. A., Y. Ming, and I. M. Held, 2014: Mechanisms of Forced Tropical Meridional Energy Flux Change. *Journal of Climate*, **28 (5)**, 1725–1742, doi:10.1175/JCLI-D-14-00165.1.

Huffman, G. J., R. F. Adler, D. T. Bolvin, and G. Gu, 2009: Improving the global precipitation record: GPCP Version 2.1. *Geophysical Research Letters*, **36 (17)**, L17 808, doi:10.1029/2009GL040000.

Hwang, Y.-T., and D. M. W. Frierson, 2010: Increasing atmospheric poleward energy transport with global warming. *Geophysical Research Letters*, **37 (24)**, L24 807, doi:10.1029/2010GL045440.

Kang, S. M., D. M. W. Frierson, and I. M. Held, 2009: The Tropical Response to Extratropical Thermal Forcing in an Idealized GCM: The Importance of Radiative Feedbacks and Convective Parameterization. *Journal of the Atmospheric Sciences*, **66 (9)**, 2812–2827, doi:10.1175/2009JAS2924.1.

Kang, S. M., I. M. Held, D. M. W. Frierson, and M. Zhao, 2008: The Response of the ITCZ to Extratropical Thermal Forcing: Idealized Slab-Ocean Experiments with a GCM. *Journal of Climate*, **21 (14)**, 3521–3532, doi:10.1175/2007JCLI2146.1.

Langen, P. L., R. G. Graversen, and T. Mauritsen, 2012: Separation of Contributions from Radiative Feedbacks to Polar Amplification on an Aquaplanet. *Journal of Climate*, **25 (8)**, 3010–3024, doi:10.1175/JCLI-D-11-00246.1.

Merlis, T. M., T. Schneider, S. Bordoni, and I. Eisenman, 2012: Hadley Circulation Response to Orbital Precession. Part I: Aquaplanets. *Journal of Climate*, **26 (3)**, 740–753, doi:10.1175/JCLI-D-11-00716.1.

Ming, Y., and V. Ramaswamy, 2011: A Model Investigation of Aerosol-Induced Changes in Tropical Circulation. *Journal of Climate*, **24**, 5125–5133.

Neelin, J. D., and I. M. Held, 1987: Modeling Tropical Convergence Based on the Moist Static Energy Budget. *Monthly Weather Review*, **115**, 3–12.

Ocko, I. B., V. Ramaswamy, and Y. Ming, 2014: Contrasting Climate Responses to the Scattering and Absorbing Features of Anthropogenic Aerosol Forcings. *Journal of Climate*, **27 (14)**, 5329–5345, doi:10.1175/JCLI-D-13-00401.1.

O'Gorman, P. A., and T. Schneider, 2008: The Hydrological Cycle over a Wide Range of Climates Simulated with an Idealized GCM. *Journal of Climate*, **21 (15)**, 3815–3832, doi:10.1175/2007JCLI2065.1.

Paynter, D., and V. Ramaswamy, 2014: Investigating the impact of the shortwave water vapor continuum upon climate simulations using GFDL global models. *Journal of Geophysical Research: Atmospheres*, **119 (18)**, 2014JD021 881, doi:10.1002/2014JD021881.

Pierrehumbert, R. T., 1995: Thermostats, Radiator Fins, and the Local Runaway Greenhouse. *Journal of the Atmospheric Sciences*, **52 (10)**, 1784–1806, doi:10.1175/1520-0469(1995)052⟨1784:TRFATL⟩2.0.CO;2.

Popp, M., and L. G. Silvers, 2017: Double and single ITCZs with and without clouds. *Journal of Climate*, doi:10.1175/JCLI-D-17-0062.1.

Privé, N. C., and R. A. Plumb, 2007: Monsoon Dynamics with Interactive Forcing. Part I: Axisymmetric Studies. *Journal of the Atmospheric Sciences*, **64 (5)**, 1417–1430, doi:10.1175/JAS3916.1.

Seo, J., S. M. Kang, and D. M. W. Frierson, 2014: Sensitivity of Intertropical Convergence Zone Movement to the Latitudinal Position of Thermal Forcing. *Journal of Climate*, **27 (8)**, 3035–3042, doi:10.1175/JCLI-D-13-00691.1.

Shekhar, R., and W. R. Boos, 2016: Improving Energy-Based Estimates of Monsoon Location in the Presence of Proximal Deserts. *Journal of Climate*, **29 (13)**, 4741–4761, doi:10.1175/JCLI-D-15-0747.1.

Sobel, A. H., J. Nilsson, and L. M. Polvani, 2001: The Weak Temperature Gradient Approximation and Balanced Tropical Moisture Waves. *Journal of the Atmospheric Sciences*, **58 (23)**, 3650–3665, doi:10.1175/1520-0469(2001)058⟨3650:TWTGAA⟩2.0.CO;2.

Voigt, A., S. Bony, J.-L. Dufresne, and B. Stevens, 2014: The radiative impact of clouds on the shift of the Intertropical Convergence Zone. *Geophysical Research Letters*, **41 (12)**, 4308–4315, doi:10.1002/2014GL060354.

Voigt, A., B. Stevens, J. Bader, and T. Mauritsen, 2013: Compensation of Hemispheric Albedo Asymmetries by Shifts of the ITCZ and Tropical Clouds. *Journal of Climate*, **27 (3)**, 1029–1045, doi:10.1175/JCLI-D-13-00205.1.

Yoshimori, M., and A. J. Broccoli, 2008: Equilibrium Response of an Atmosphere–Mixed Layer Ocean Model to Different Radiative Forcing Agents: Global and Zonal Mean Response. *Journal of Climate*, **21 (17)**, 4399–4423, doi:10.1175/2008JCLI2172.1.

Yoshimori, M., and A. J. Broccoli, 2009: On the link between Hadley circulation changes and radiative feedback processes. *Geophysical Research Letters*, **36 (20)**, L20 703, doi:10.1029/2009GL040488.

Yoshioka, M., N. M. Mahowald, A. J. Conley, W. D. Collins, D. W. Fillmore, C. S. Zender, and D. B. Coleman, 2007: Impact of Desert Dust Radiative Forcing on Sahel Precipitation: Relative Importance of Dust Compared to Sea Surface Temperature Variations, Vegetation Changes, and Greenhouse Gas Warming. *Journal of Climate*, **20 (8)**, 1445–1467, doi:10.1175/JCLI4056.1.

LIST OF TABLES

	Tropics [$\mathrm{W\,m^{-2}}$]		Extratropics [$\mathrm{W\,m^{-2}}$]		
Perturbation	Shortwave	Longwave	Shortwave	Longwave	Total [$\mathrm{W\,m^{-2}}$]
T5	-0.57 (21.5 %)	-2.42 (90.9 %)	-0.17 (6.3 %)	0.46 (−17.1 %)	-2.66
T10	-1.06 (18.5 %)	-4.87 (84.9 %)	-0.34 (6.0 %)	0.43 (−7.6 %)	-5.73
T15	-1.30 (17.3 %)	-6.10 (80.9 %)	-0.43 (5.7 %)	0.25 (−3.3 %)	-7.54
T18	-1.32 (17.4 %)	-6.16 (81.2 %)	-0.48 (6.3 %)	0.32 (−4.3 %)	-7.58
E5	-0.29 (25.0 %)	-0.79 (69.3 %)	-0.32 (27.7 %)	0.15 (−22.2 %)	-1.15
E10	-0.58 (34.1 %)	-1.56 (91.3 %)	-0.55 (32.0 %)	0.94 (−55.0 %)	-1.71
E15	-0.77 (28.3 %)	-2.43 (88.7 %)	-0.70 (25.4 %)	1.13 (−41.1 %)	-2.74
E18	-0.91 (33.1 %)	-2.77 (101.1 %)	-0.73 (26.5 %)	1.70 (−62.9 %)	-2.74

TABLE 1. Decomposition of total difference in hemispheric asymmetry in net column heating into components due to differences in tropical and extratropical asymmetries in net shortwave radiation at TOA and outgoing longwave radiation for cases using the default convective relaxation time. Percentages in parentheses represent the percent of the total the contribution makes up.

LIST OF FIGURES

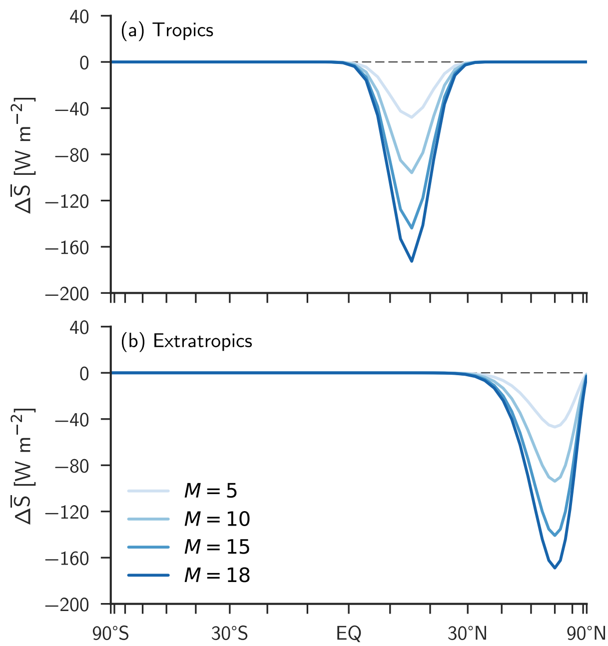

FIG. 1. Annual mean perturbation to incoming solar radiation. Panel (a) shows the tropical perturbation; panel (b) shows the extratropical perturbation.

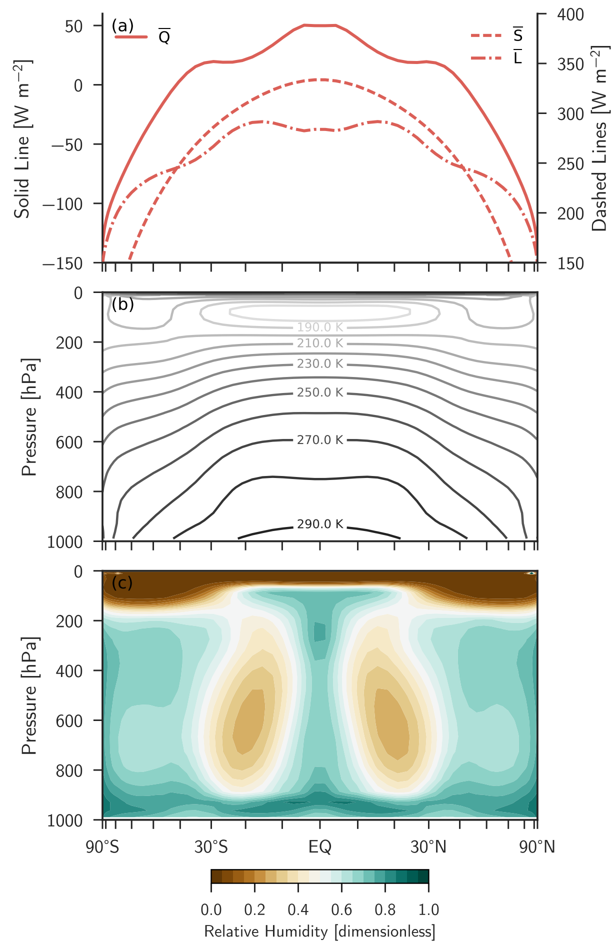

890 FIG. 2. Zonal and time mean net column heating (solid line), net shortwave radiation (dashed line), and outgoing longwave radiation at TOA (dashed-dotted line) (a), temperature (b), and relative humidty (c) in the control simulation with the default value of the convective relaxation time.

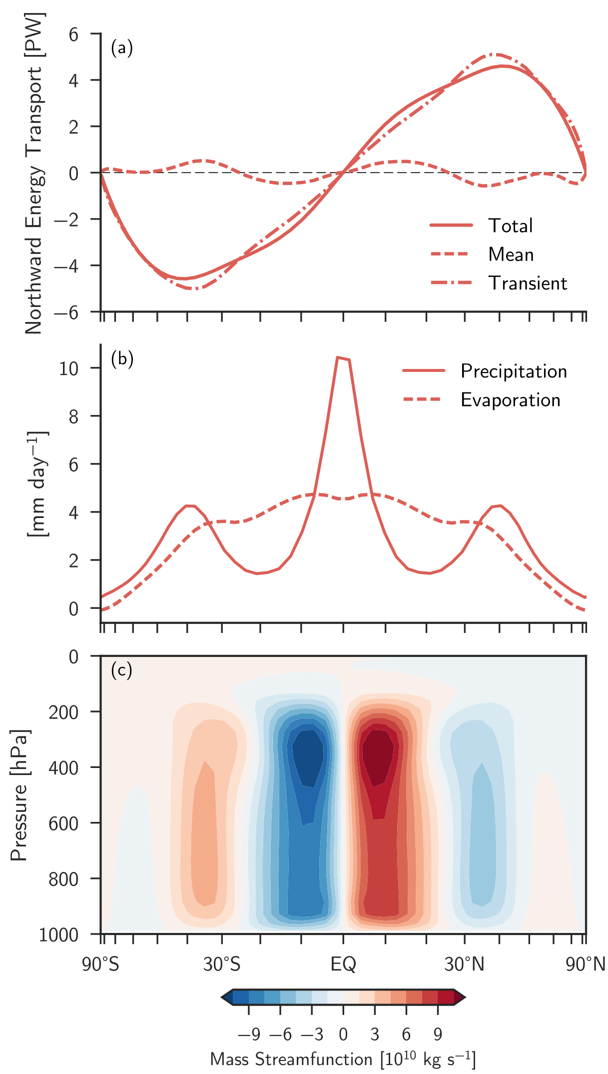

FIG. 3. Zonally and vertically integrated moist static energy flux decomposed into mean and transient components (a); zonal and time mean precipitation rate and evaporation rate (b); and mean mass streamfunction (c) from the control simulation with default convective relaxation time.

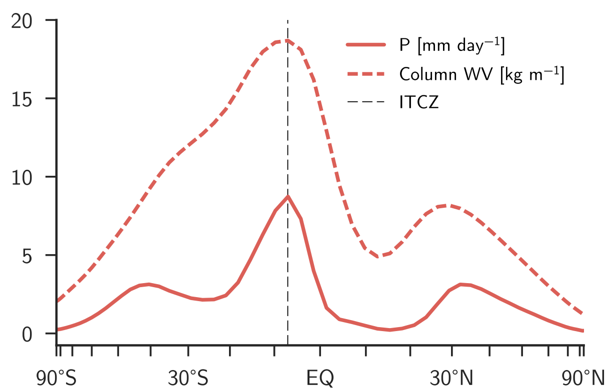

FIG. 4. Zonal and time mean precipitation rate and column integrated water vapor for case with the default convective relaxation time, interactive water, and a $M = 15\,\mathrm{W m^{-2}}$ perturbation imposed in the tropics. The ITCZ latitude is denoted by the black dashed line.

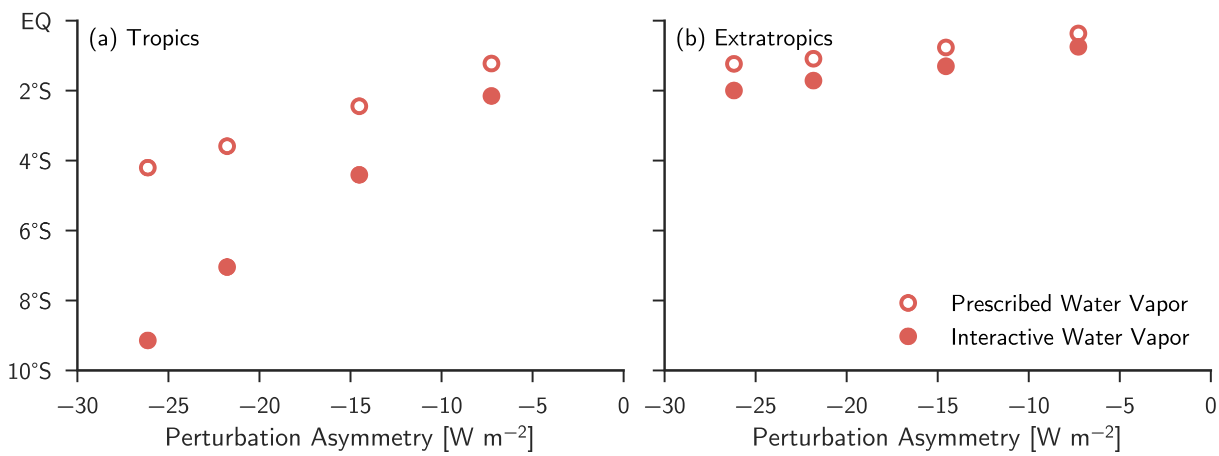

FIG. 5. ITCZ latitude plotted against the hemispheric-asymmetry in absorbed solar insolation for cases with the default convective relaxation time and interactive water vapor and radiation (filled symbols) or presribed water vapor-radiation interaction (closed symbols). Panel (a) shows the results of cases with the perturbation imposed in the tropics and panel (b) shows the results of cases with the perturbation imposed in the extratropics. Circles represent cases where the forcing is imposed in the tropcis, while squares represent cases where the forcing is imposed in the extratropics.

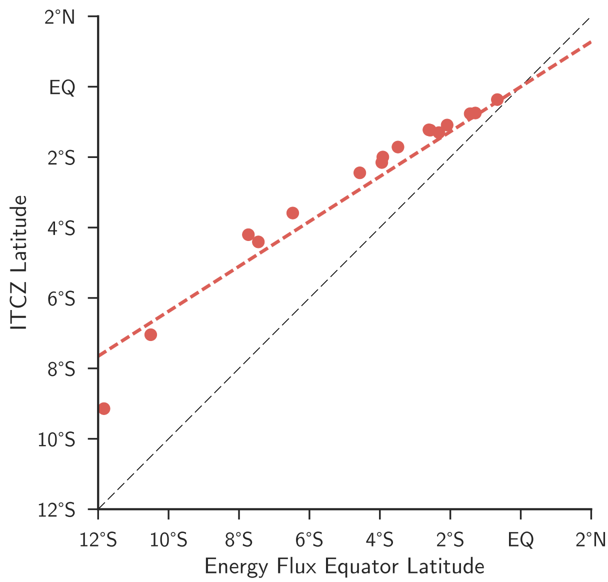

FIG. 6. ITCZ latitude versus energy flux equator latitude for cases with the default convective relaxation time. The black line is the one-to-one line; the red dashed line is a line of best fit through the origin (slope equals 0.64 and coefficient of determination is $r^2 = 0.95$).

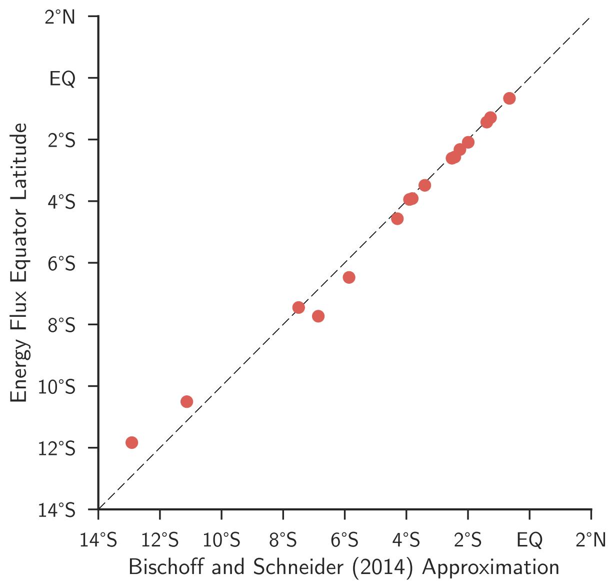

FIG. 7. True energy flux equator latitude plotted against the diagnosed energy flux equator latitude by Equation 10 for all cases with the default convective relaxation time. The black line represents a one-to-one correspondence. A line of best fit through the origin has a slope of 0.98 and a coefficient of determination of $r^2 = 0.98$.

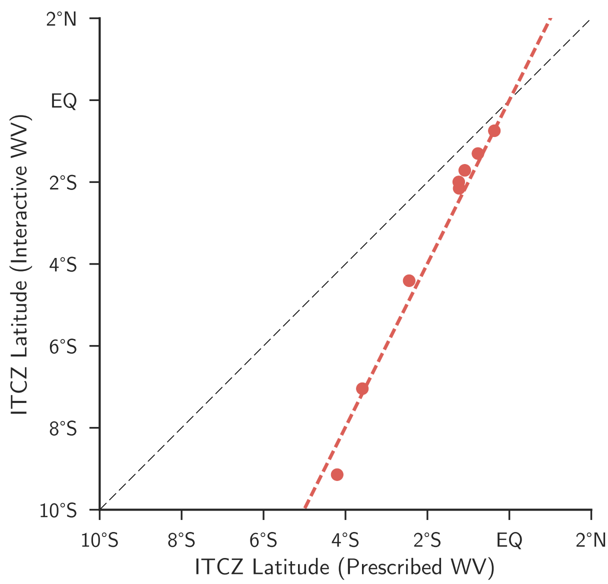

FIG. 8. ITCZ position in interactive water cases versus ITCZ position in prescribed water cases with the default convective relaxation time. The colored dashed line is fitted to pass through the origin and minimize least squares error from the points; it has a slope of 2.00 and a coefficient of determination of $r^2 = 0.98$.

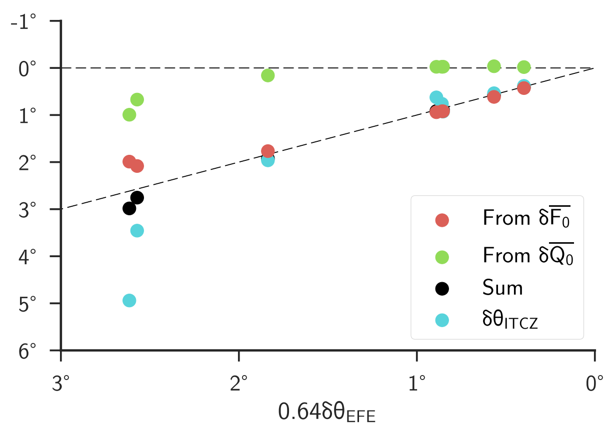

915 FIG. 9. Decomposition of the difference in energy flux equator position between cases with interactive water vapor and radiation and cases with prescribed water vapor-radiation interaction, with the default convective relaxation time. The diagonal black dashed line represents a one-to-one correspondence.

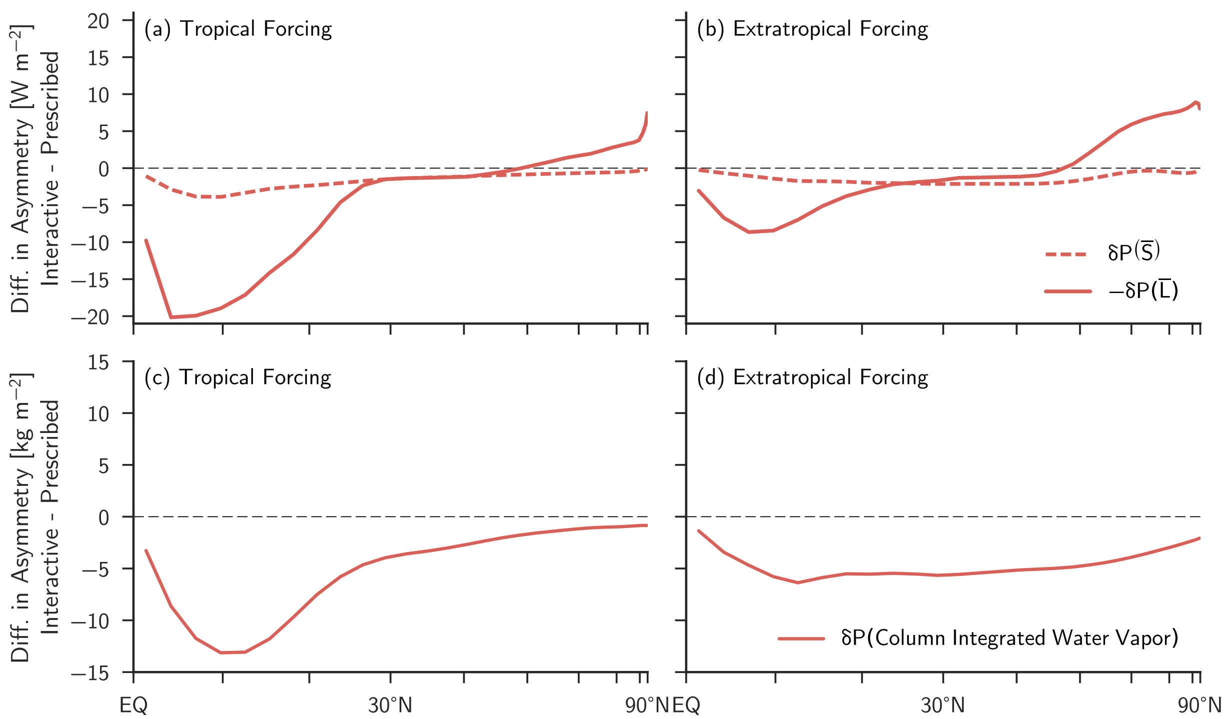

918 FIG. 10. Difference in point-wise asymmetry in net column heating between cases with interactive water
919 and prescribed water, for a perturbation of magnitude $M = 15\,\mathrm{Wm}^{-2}$ using the default convective relaxation
920 time decomposed into components due to net shortwave radiation at TOA (dashed line) and outgoing longwave
921 radiation (dashed-dotted line). Panel (a) shows results from a case with the perturbation imposed in the tropics;
922 panel (b) shows results from a case with the perturbation imposed in the extratropics. Panels (c) and (d) show
923 the difference in point-wise asymmetry in column integrated water vapor seen by the radiation code between the
924 interactive and prescribed water cases represented in panels (a) and (b).

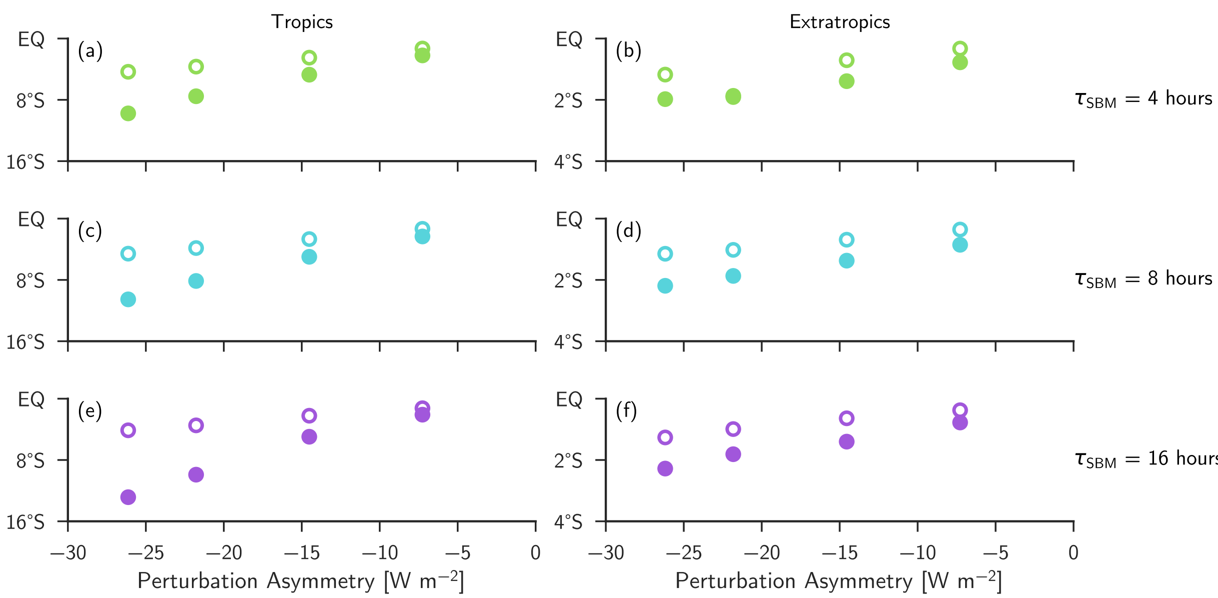

FIG. 11. ITCZ position plotted against the hemispheric-asymmetry in absorbed solar insolation for cases with interactive water vapor and radiation (filled symbols) or prescribed water vapor-radiation interaction (closed symbols) with varying convective relaxation times (green symbols for $\tau_{\mathrm{SBM}} = 4\,\mathrm{h}$, blue symbols for $\tau_{\mathrm{SBM}} = 8\,\mathrm{h}$, and purple symbols for $\tau_{\mathrm{SBM}} = 16\,\mathrm{h}$). The left column shows the results of cases with the perturbation imposed in the tropics and the right column shows the results of cases with the perturbation imposed in the extratropics. Note the difference in the scale of the y-axis between the two columns.

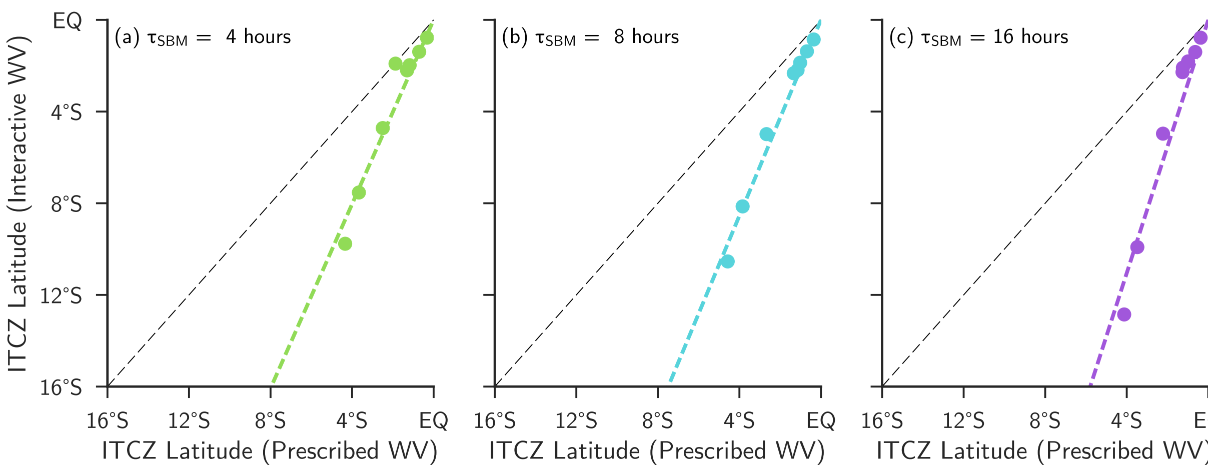

931 FIG. 12. ITCZ position in interactive water cases versus ITCZ position in prescribed water cases with varying convective relaxation time. The colored dashed lines are fits through least squares regression. Panel (a) uses a convective relaxation time of 4 h and the line of best fit has a slope of 2.01 and a coefficient of determination of $r^2 = 0.93$; panel (b) uses a convective relaxation time of 8 h and the line of best fit has a slope of 2.14 and a coefficient of determination of $r^2 = 0.98$; and panel (c) uses a convective relaxation time of 16 h and the line of best fit has a slope of 2.76 and a coefficient of determination of $r^2 = 0.94$.

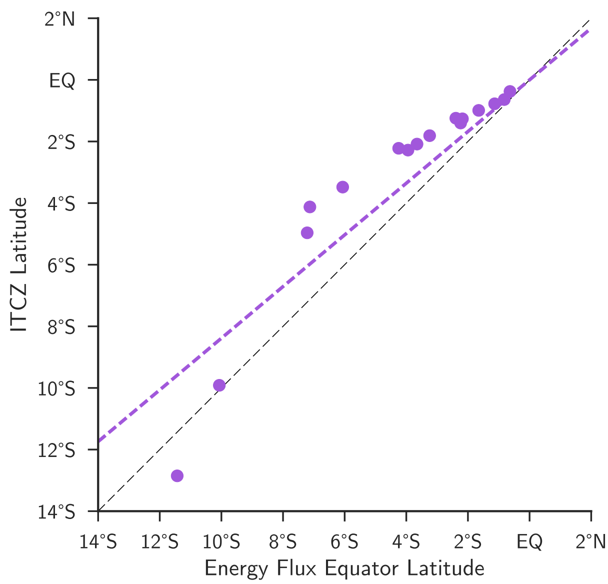

FIG. 13. ITCZ latitude versus energy flux equator latitude for the case with a convective relaxation time of 16 h. The black line represents the one-to-one line; the colored dashed line is the line of best fit through the origin (slope equals 0.84 and the coefficient of determination is $r^2 = 0.86$).

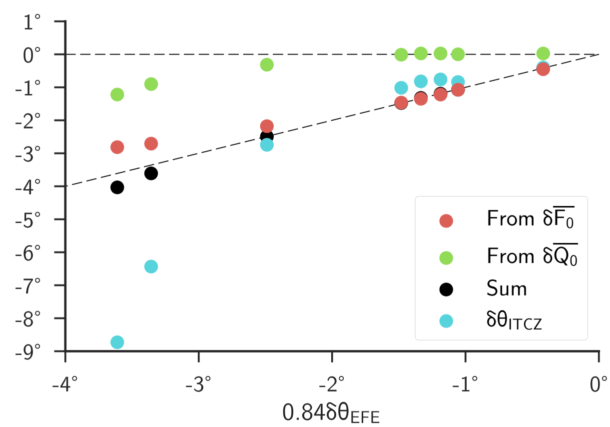

FIG. 14. Decomposition of the difference in energy flux equator position between cases with interactive water vapor and radiation and cases with prescribed water vapor-radiation interaction; all results here are from simulations with a convective relaxation time of 16 h. The diagnonal black dashed line represents a one-to-one correspondence.

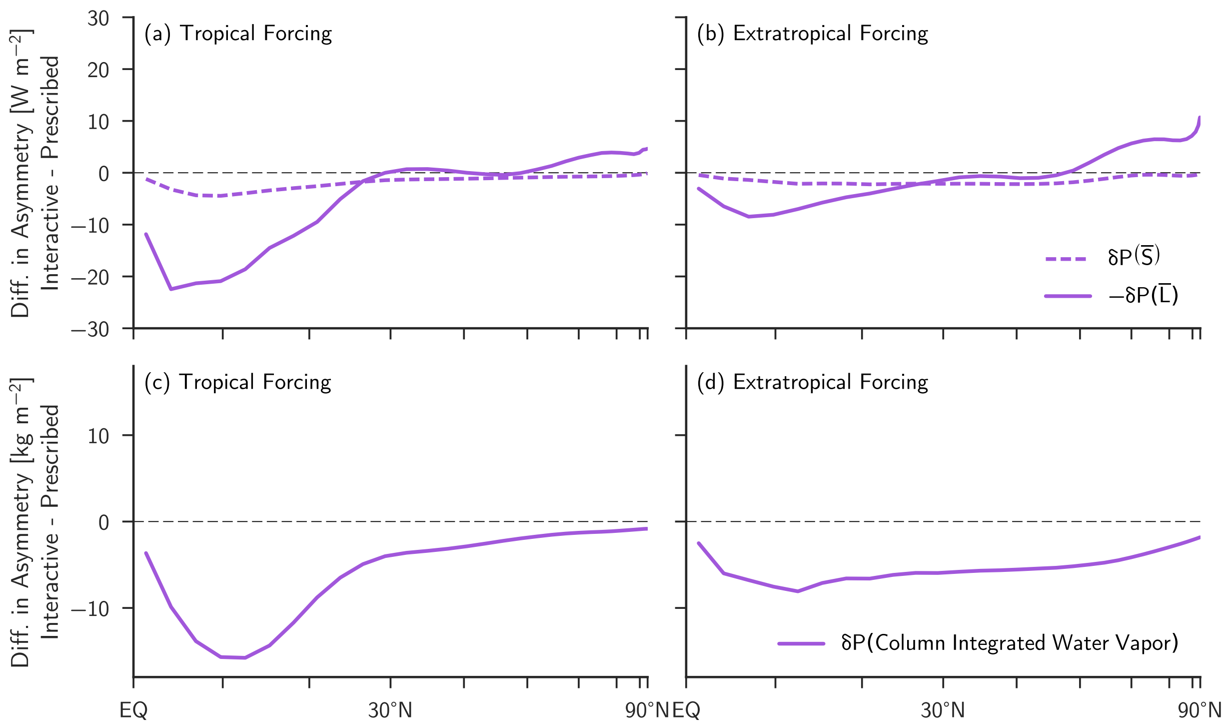

944 FIG. 15. Difference in point-wise asymmetry in net column heating between cases with interactive water
945 and prescribed water, for a perturbation of magnitude $M = 15\,\mathrm{W\,m^{-2}}$, and convective relaxation time of 16
946 hours decomposed into components due to net shortwave radiation at TOA (dashed line) and outgoing longwave
947 radiation (dashed-dotted line). Panel (a) shows results from a case with the perturbation imposed in the tropics;
948 panel (b) shows results from a case with the perturbation imposed in the extratropics. Panels (c) and (d) show
949 the difference in point-wise asymmetry in column integrated water vapor seen by the radiation code between the
950 interactive and prescribed water cases represented in panels (a) and (b).

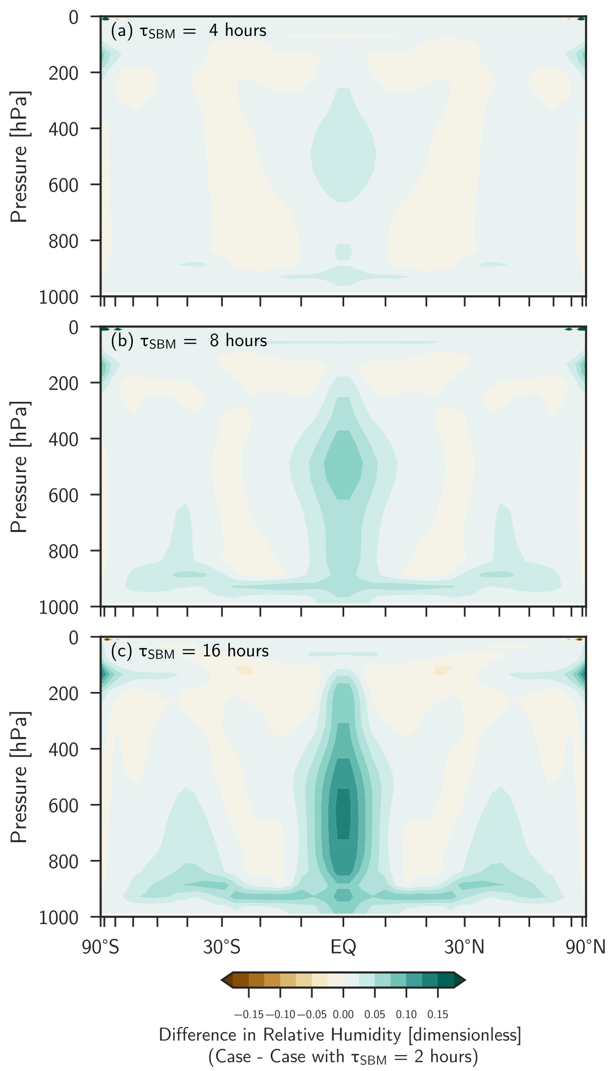

FIG. 16. Difference in symmetrized relative humidity between symmetric control simulations with convective relaxation times of 4, 8, and 16 hours and the control simulation with the default convective relaxation time (2 hours) [panels (a), (b), and (c) respectively].

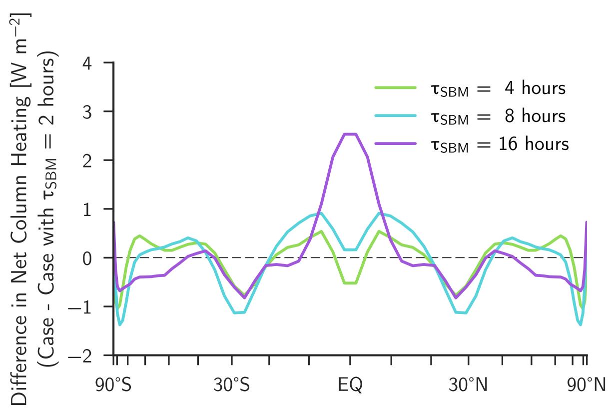

FIG. 17. Difference in symmetrized net column heating between symmetric control simulations with convective relaxation times of 4, 8, and 16 hours and the control simulation with the default convective relaxation time (2 hours).